catalysts

MDPI

*Article*

# Facile Synthesis of Sillén-Aurivillius Layered Oxide $Bi_7Fe_2Ti_2O_{17}Cl$ with Efficient Photocatalytic Performance for Degradation of Tetracycline

**Yan Gu, Fang Yu, Jikun Chen and Qinfang Zhang ***

School of Materials Science and Engineering, Yancheng Institute of Technology, Yancheng 224001, China; ygu9705@gmail.com (Y.G.); yufangjenny@sina.com (F.Y.); wwa912251@gmail.com (J.C.)
* Correspondence: qfangzhang@gmail.com

**Abstract:** The development of an efficient and environment-friendly photocatalyst for antibiotics degradation is of great significance and still remains a major challenge. Herein, a novel Sillén-Aurivillius layered oxide $Bi_7Fe_2Ti_2O_{17}Cl$ is successfully synthesized via a one-step flux route (noted as F-BFTOC) and solid-state reaction (noted as S-BFTOC). The as-prepared F-BFTOC manifests the enhanced visible-light photocatalytic performance towards tetracycline (TC) degradation compared with $Bi_4NbO_8Cl$ and its degradation efficiency reaches 90% within 90 min. Additionally, the proposed degradation pathway and photocatalytic mechanism are systematically investigated by liquid chromatography tandem-mass spectrometry (HPLC-MS), active species trapping test, electron spin resonance (ESR) and first-principles calculations. The superior degradation of antibiotics is primarily derived from the photo-generated $h^+$, and radical $\cdot O_2^-$ as the dominant active species. More importantly, the F-BFTOC exhibits excellent cycle stability and TC is ultimately transformed into non-toxic open-loop products. Simultaneously, Rhodamine B (RhB) as a typical organic pollutant is further employed to evaluate the photocatalytic activity of F-BFTOC, and 98% of the degradation efficiency is achieved. BFTOC as a multifunctional photocatalyst for pollutant degradation offers a new insight for Sillén-Aurivillius photocatalytic in the field of water purification.

**Keywords:** $Bi_7Fe_2Ti_2O_{17}Cl$; photocatalyst; tetracycline; degradation mechanism



**Citation:** Gu, Y.; Yu, F.; Chen, J.; Zhang, Q. Facile Synthesis of Sillén-Aurivillius Layered Oxide $Bi_7Fe_2Ti_2O_{17}Cl$ with Efficient Photocatalytic Performance for Degradation of Tetracycline. *Catalysts* **2022**, *12*, 221. https://doi.org/10.3390/catal12020221

Academic Editors: Vincenzo Vaiano and Olga Sacco

Received: 1 January 2022
Accepted: 9 February 2022
Published: 15 February 2022



## 1. Introduction

Currently, a variety of contaminations out of water lead to the accumulation of toxic pollutants in environment, which seriously affects waterbody biodiversity and even the health of humans [1,2]. In particular, water pollutants are attributable to immoderate antibiotics, which have attracted significant attention in recent decades. Very limited amounts of antibiotics are able to be eliminated by conventional biological and chemical technologies [3–5]. Tetracycline (TC) as a class of representative antibiotic is impossible to be completely metabolized by natural degradation and biodegradability. A portion of the high toxicity of the intermediate products of TC is excreted, which poses a huge threat to the aquatic ecosystem [6]. Therefore, the development of a simple and effective strategy to degrade subaqueous TC is of considerable importance.

Several methods have been studied and applied to degrade antibiotics specifically, involving chemical oxidation, biotechnology, adsorption, electrochemical process, and photodegradation [7]. Of all the existing treatments, photocatalytic technology owing to low cost, excellent sustainability, and high efficiency is recognized as a promising strategy to address environmental issues. Photocatalytic technology directly utilizes solar energy to thoroughly degrade and eventually mineralize antibiotics from wastewater [8–10]. Yet, semiconductors are used as photocatalysts to eliminate the organic pollutants from wastewater, such as zinc oxide (ZnO), titanium dioxide ($TiO_2$), g-$C_3N_4$, and so on [11–16]. However, the wide band gap of semiconductors and the slow rate of photogeneration of electron-hole

pairs causes low quantum efficiency restricting the photocatalytic efficiency under visible light [17–19]. Bi-based photocatalysts including Sillén structures BiOX (X = Cl, Br, I) [20], Aurivillius structure $Bi_2WO_6$ [21], $Bi_2MoO_6$ [22], $Bi_3TiNbO_9$ [23], and Sillén-Aurivillius structure $Bi_4NbO_8Cl$ [24], $Bi_4Ti_{0.5}W_{0.5}O_8Cl$ [25] have a unique valence band formed by hybridization of Bi-6*s* and O-2*p* orbitals [26] resulting in remarkable photocatalytic activity. Among the conventional Bi-based photocatalysts, Sillén-Aurivillius structure of photocatalysts consist of halide, fluorite and perovskite slabs [27]. Especially, selective cation and/or anion substitution for the perovskite slabs in Sillén-Aurivillius structure provides broad structural variations to regulate the optical and electrochemical properties, which is able to be performed significantly in photocatalytic water treatment [28]. Surprisingly, there are few studies that focus on a Sillén-Aurivillius structure of Bi-based photocatalysts for antibiotics photodegradation [29,30]. In recent studies, Xu et al. [31] synthesized $Bi_4NbO_8Cl$ nanosheets by a molten-salt growth method, but only 60% of TC was degraded by $Bi_4NbO_8Cl$ within 240 min irradiation. Wu et al. [32] fabricated $Bi_4NbO_8Cl$ and heterostructured $Bi/Bi_4NbO_8Cl$ via in-situ solvothermal method, 30% of TC was degraded by $Bi_4NbO_8Cl$ within 180 min irradiation, and 50% of TC was degraded by $Bi/Bi_4NbO_8Cl$ under the same conditions. Because of the unsatisfactory degradation performance, new Bi-based Sillén-Aurivillius catalysts with better photocatalytic properties than $Bi_4NbO_8Cl$ are required to be developed.

As we all know, Sillén-Aurivillius phases have the general formula $(Bi_2O_2)_2Cl$ ($A_{n-1}M_nO_{3n+1}$), where $n$ stands for the number of perovskite layers. For instance, $Bi_4NbO_8Cl$ belongs to the Sillén-Aurivillius phases with $n$ = 1. The electronic properties of perovskites can be altered via changing their dimensionality through increasing the value of $n$ owing to the quantum confinement effect; furthermore, modifying the chemical composition of perovskites via alloying or doping also greatly changes their transport properties. To achieve efficient and stable visible-light-driven photocatalysts, it worth investigating the Sillén-Aurivillius phases with multi-perovskite layers ($n$ > 1), in which the band alignment and carrier transport might modulate by their dimensionality.

Herein, a novel Bi-based Sillén-Aurivillius $Bi_7Fe_2Ti_2O_{17}Cl$ ($n$ = 4) was successfully obtained through a one-step flux method (noted as F-BFTOC, Figure 1a). Compared with the traditional solid phase method, the excellent properties of the samples prepared by molten salt method were discovered. For the first time, F-BFTOC was used for the visible-light-driven degradation of TC, and an excellent degradation efficiency of 90% was achieved within 90 min under visible light irradiation. The intermediate products of TC were tracked by the HPLC-MS, and the degradation pathway was deduced based on ESR. The photo-generated $h^+$ and radical $\cdot O_2^-$ as the dominant active species contributed to the degradation of TC, and the ·OH was peripheral to degradation. More importantly, the high efficiency of F-BFTOC could be maintained after three cycles and F-BFTOC even exhibited a significant detoxification. Moreover, organic contaminant (RhB) was tested to evaluate the prospects of F-BFTOC for organic wastewater, the degradation efficiency was up to 98%. BFTOC gave a new perspective of Sillén-Aurivillius structural Bi-based materials for the remediation of environmental pollutants.

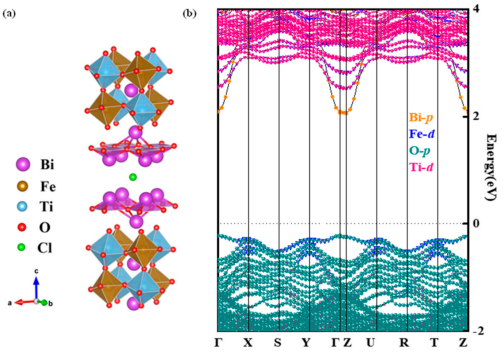


**Figure 1.** (**a**) A novel Sillén-Aurivillius layered oxide $Bi_7Fe_2Ti_2O_{17}Cl$ and (**b**) its calculated band structure.

## 2. Results and Discussion

### *2.1. Phase and Microstructure*

S-BFTOC powders were prepared using the conventional solid-state reaction and calcined at 750 °C for 12 h, and F-BFTOC powders were synthesized through liquid-state flux method. The X-ray diffraction (XRD) was employed to identify purity and crystal phase of as-fabricated samples. Figure 2a displayed the XRD patterns of S-BFTOC and F-BFTOC, and the diffraction peaks at 20.22°, 30.56°, 32.638°, which could be identified as the (004), (116) and (020) crystal planes, corresponding to the previously reported results [33]. In addition, the sharp peaks of F-BFTOC indicated an excellent crystallinity and high purity of the material, confirming the successful formation of the BFTOC. As compared, XRD measurements (Figure S1a) were done for F-BNOC and S-BNOC samples. We have successfully synthesized the BNOC samples through comparing the XRD patterns with the previous work [34].

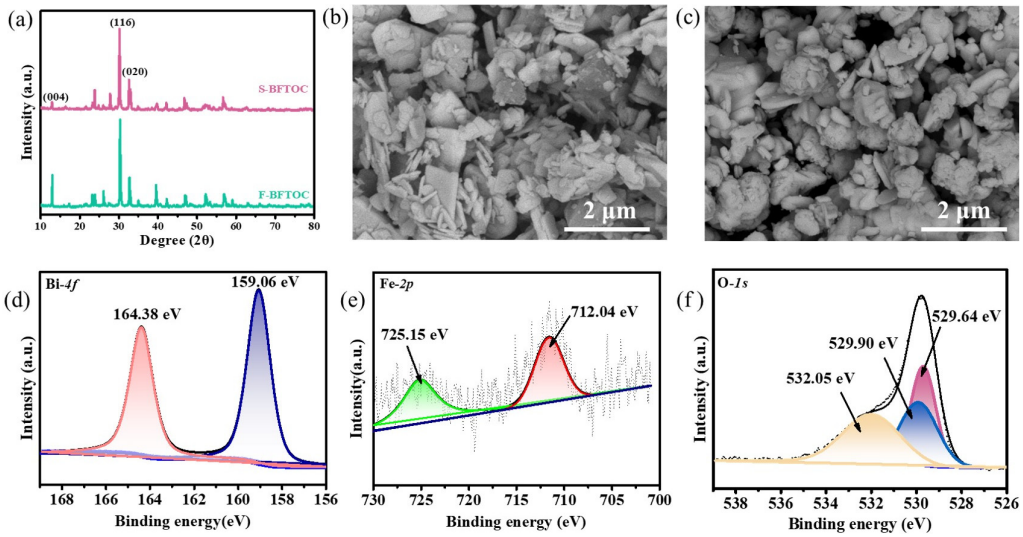


**Figure 2.** (**a**) XRD patterns of F-BFTOC and S-BFTOC, respectively; (**b**,**c**) SEM images of F-BFTOC and S-BFTOC, respectively; (**d**–**f**) High resolution XPS spectra of Bi-4*f*, Fe-2*p*, and O-1*s* of F-BFTOC, respectively.

The microstructure of the as-prepared photocatalysts was observed by scanning electron microscopy (FE-SEM). The characterized morphology of nanosheet structure of F-BFTOC was clearly depicted in Figure 2b, and S-BFTOC was heterogeneous and had agglomeration in Figure 2c. The large area of sheet at μm level of F-BFTOC was able to expose more active sites and promote the mass transfer process, which in a certain sense improved the photocatalytic activity [35]. X-ray photoelectron spectroscopy (XPS) analysis was conducted to measure the surface electronic valances and elemental composition of the photocatalyst. Figure S2 presented the survey spectra of F-BFTOC corresponding to Bi, Fe, Ti, O and Cl elements. Figure 2d showed Bi-4*f* spectrum at 159.06 eV (Bi-4$f_{7/2}$) and 164.38 eV (Bi-4$f_{5/2}$), which was attributed to $Bi^{3+}$ [36]. In the Fe-2*p* spectrum (Figure 2e), two main peaks at 712.05 eV and 725.15 eV could be ascribed to Fe-2$p_{1/2}$ and Fe-2$p_{3/2}$, respectively [37]. The reason for the very weak signal from Fe may be the uneven distribution of Fe elements on the surface. The Ti-2*p* spectrum was displayed in Figure S3, and could be deconvoluted into two peaks. The binding energy of 457.82 eV and 465.81 eV belonged to the Ti-2$p_{1/2}$, Ti-2$p_{3/2}$, respectively, which was in accordance with the representative characteristics of Ti (IV) in F-BFTOC [38]. In the Cl-2*p* region (Figure S4), two peaks of F-BFTOC at 198.08 eV and 199.70 eV were assigned to Cl-2$p_{3/2}$ and Cl-2$p_{1/2}$, which demonstrated the existence of $Cl^-$ from F-BFTOC [39]. The high-resolution O-1*s* XPS spectrum of F-BFTOC could be de-convoluted into three peaks. The peaks situated at 532.05 eV, 529.90 eV, 529.64 eV, corresponding to $[Bi_2O_2]^{2+}$ block and lattice oxygen, respectively.

### 2.2. Optical Property

The optical bandgap and photo-absorption of F-BFTOC was examined though UV-Vis diffuse reflectance spectroscopy (DRS), as displayed in Figure 3a. F-BFTOC possessed a strong absorption in the visible-light region and the absorption edge was approximately 500 nm. The bandgap value of F-BFTOC was calculated by the well-known Kubelka-Munk formula depicted as follows [40,41]:

$$\alpha h\upsilon = C(h\upsilon - E_g)^n \quad (1)$$

where $\alpha$ was the absorption coefficient values, h was Planck's constant, $\upsilon$ was the radiation frequency, C was a constant and $E_g$ was the energy gap. Since F-BFTOC was a direct bandgap semiconductor as shown in Figure 1b, the value of n was taken as $\frac{1}{2}$, the band gap ($E_g$) was obtained by the plots of $(\alpha h\upsilon)^2$ vs. photo energy. As shown in Figure 3b, the $E_g$ value of F-BFTOC was confirmed to be 2.64 eV, suggesting that the narrow band gap of F-BFTOC could act as a significant photocatalyst in the degradation of contaminations under visible light irradiation. We have also done the optical band gap measurement for BNOC samples, which were shown in Figure S1b. The accurate band alignments of F-BFTOC and F-BNOC were determined by VB-XPS in combination with the $E_g$ results (Figure 3c). The valence band (VB) of F-BFTOC was speculated to be +2.28 eV, and the conduction band (CB) maxima of F-BFTOC was calculated to be −0.36 eV, as depicted in Figure 3d. The values of $E_{VB}$ and $E_{CB}$ of BNOC was found to be 1.91 and −0.39 eV (NHE), respectively, according to the literature survey [24]. The energy band position of photocatalyst was attained, which was conducive to the investigation of the catalytic reaction mechanism.

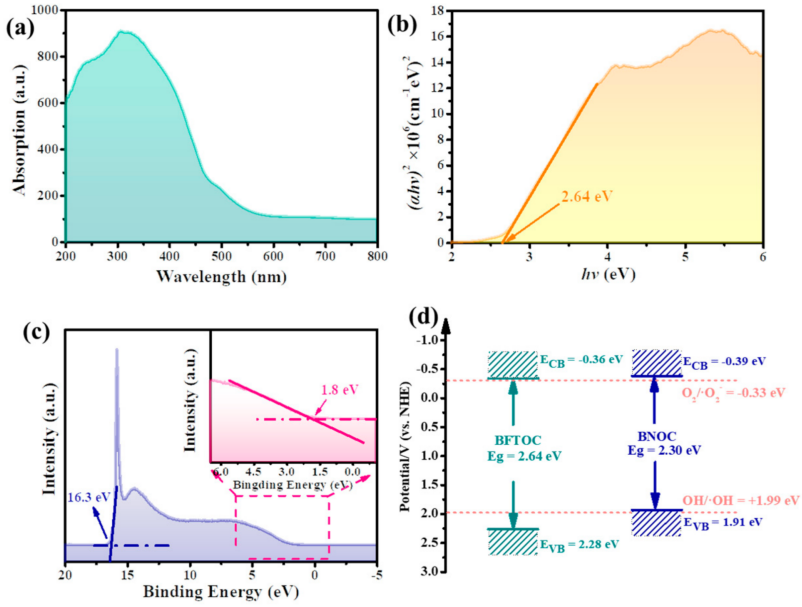


**Figure 3.** (**a**) UV-vis DRS spectrum of F-BFTOC; (**b**) Tauc's band-gap plots of F-BFTOC; (**c**) VB XPS spectrum and energy-band alignment diagrams (insert) of F-BFTOC. (**d**) The band alignments of F-BFTOC and F-BNOC, respectively.

### 2.3. Band Structures

The atomic and orbital revolved band structures (Figure 1b) was obtained by DFT calculations. The Fermi level is set to zero and marked by a vertical dashed line. From the previous report we know that the conduction band minimum (CBM) is mainly composed of a mixture of Bi-6*p* and Nb-4*d* states and the valence band maximum (VBM) is predominately contributed by O-2*p* states for BNOC. In BFTOC, the O-2*p* states and Fe-3*d* states importantly contribute for the formation of the VBM, while the CBM is dominated by the

Bi-6*p* states. The hybridization of O-2*p* and Fe-3*d* states in BFTOC introduces the larger dispersion of band structures near the VBM compared to BNOC, which contributes to the efficient oxidization of water by the holes populated on the stable oxygen anions.

### *2.4. Photocatalytic Activity*

The estimation of photocatalytic performance of F-BFTOC, S-BFTOC, F-BNOC and S-BNOC photocatalysts was performed by the degradation of TC and RhB dyes under the visible light irradiation. After the achievement of the adsorption equilibrium in dark, the photocatalytic reactions were carried out. As exhibited in Figure 4a, the blank experiment indicated that the self-photolysis of TC could be ignored. Compared with S-BFTOC, the adsorption capacity of F-BFTOC to pollutants was greatly improved because of the larger surface area prepared by the molten salt method [35]. The concentration of TC obviously declined by assistance with photocatalysts, F-BNOC and S-BNOC exhibited the poor photocatalytic activity. F-BFTOC exhibited the highest photocatalytic capability, and nearly 90% of TC was eliminated after 90 min of visible-light irradiation. The degradation efficiency of BNOC was distinctly inferior to that of BFTOC, revealing that BFTOC accelerated the separation of electron-hole pairs for boosting the photocatalytic performance. Obviously, the photocatalytic capability of BFTOC was much better than BNOC prepared by Xu et al. [31]. Thus, the TOC removal of TC may be larger than that of Xu's work. The photocatalytic degradation kinetics of F-BFTOC, S-BFTOC, F-BNOC and S-BNOC were further explored by the pseudo-first-order kinetics model and pseudo-second-order kinetics model [42], and were given in the following:

$$ln(C_0/C_t) = k_1 t \quad (2)$$

$$t/(ln(C_0/C_t)) = t/a + 1/\left(k_2\, a^2\right) \quad (3)$$

where $k_1$ was the pseudo-first-order kinetic rate constant ($min^{-1}$), $t$ was the irradiation time, $k_2$ was pseudo-second-order kinetic rate constant ($mol^{-1}$ $dm^3$ $s^{-1}$), $C_0$ was the initial concentration of the contaminations (mg/L), $C_t$ was the concentration of contaminations at various irradiation time (min), a was the value of $ln$ $(C_0/C_t)$ at equilibrium. The kinetic linear fitting curves were displayed in Figure 4b, the TC degradation reaction could be described as the pseudo-second-order model equation, and kinetics data were summarized in Table S1. The F-BFTOC possessed the highest $k_2$ value of 0.058 $mol^{-1}$ $dm^3$ $s^{-1}$, which was 4-fold higher than those of F-BNOC for TC degradation. Remarkably, the photocatalytic activity of BFTOC was better than BNOC.

In Figure 4g, the absorption intensity of TC was reduced, which confirmed that TC was gradually degraded and completely decomposed into small-molecule products.

To optimize the photocatalytic performance of F-BFTOC, the other parameter on the photodegradation activities of F-BFTOC, TC concentration, was investigated. As shown in Figure 4c,d, with the increased TC concentration (10 mg/L, 20 mg/L, 30 mg/L, 40 mg/L, 50 mg/L), the removal rate of F-BFTOC to tetracycline hydrochloride decreased gradually. The concentration of tetracycline hydrochloride rose up to 50 mg/L, the removal rate of F-BFTOC could still reach 66% in 120 min. Therefore, F-BFTOC was capable of still showing excellent degradation performance for the high concentration of tetracycline hydrochloride.

Beyond that, the photocatalytic ability of photocatalyst was further studied via the degradation of RhB under visible-light irradiation, RhB was a typical organic molecule that was difficult to be completely removed. As a control, the degradation of RhB over photocatalyst under dark condition was negligible (Figure 4e). The RhB was significantly degraded when the photocatalyst was added, and 98% of RhB was removed by F-BFTOC within 90 min of reaction, further suggesting the outstanding photocatalytic activity of BFTOC for the efficient degradation of organic pollutants. The highest RhB degradation for F-BFTOC was achieved, being 1.31 more than F-BNOC. The photocatalytic degradation kinetics of F-BFTOC, S-BFTOC, F-BNOC and S-BNOC for RhB were investigated by the pseudo-first-order kinetics model and pseudo-second-order kinetics model, and kinetics data were summarized in Table S2. In Figure 4e, f, the degradation system with the removal

of RhB well followed the pseudo-first-order kinetic model. The $k_1$ value of 0.038 $min^{-1}$ was noted for F-BFTOC photocatalyst, which was 2.71 times higher than that of F-BNOC. The absorption spectra of RhB over F-BFTOC illustrated that F-BFTOC nanosheets could effectively degrade RhB. Therefore, F-BFTOC greatly improved the separation and transfer efficiency of photo-induced carriers, and F-BFTOC with higher surface areas possessed more active sites, thereby enhancing the photocatalytic performance. F-BFTOC was selected as the optimum photocatalyst.

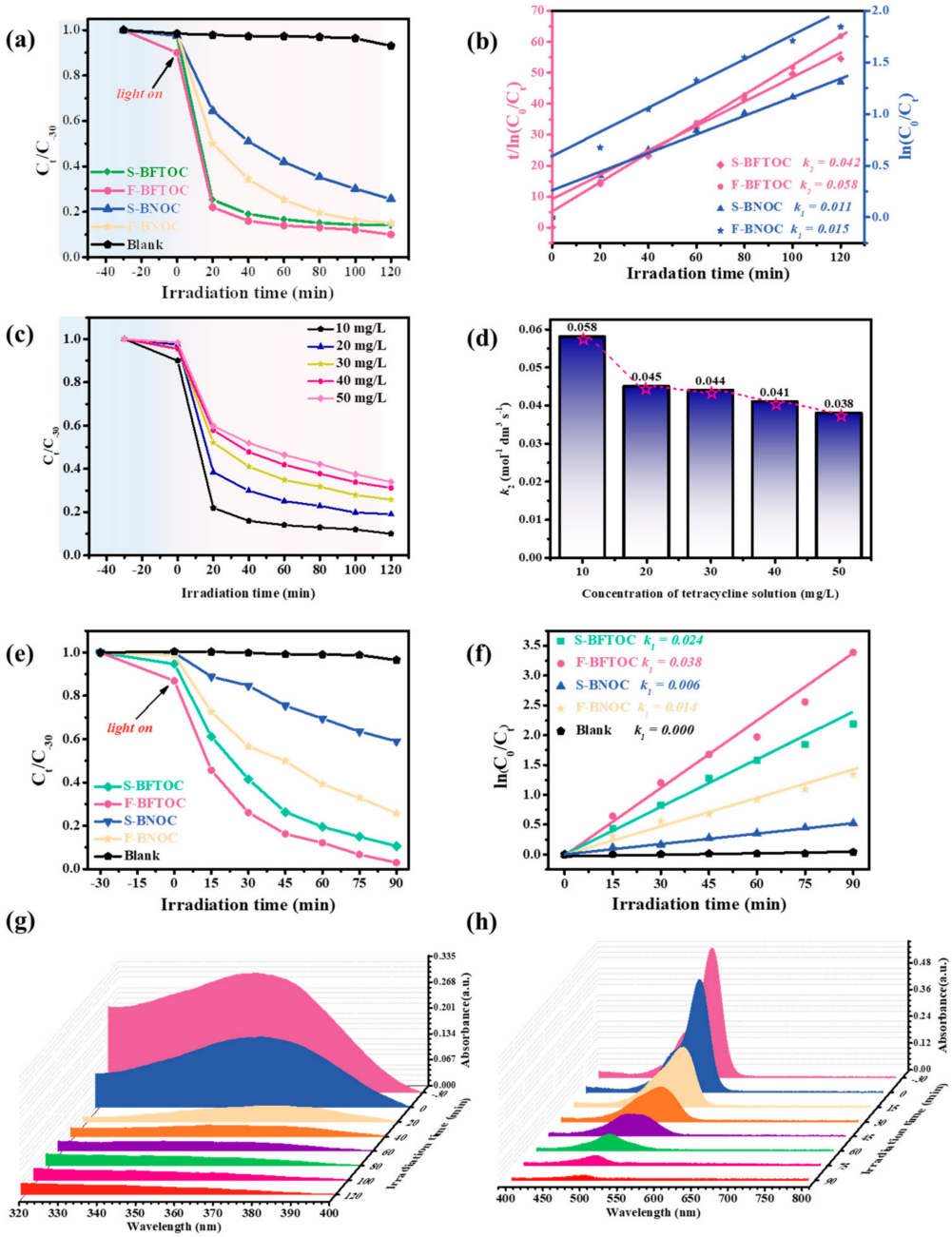


**Figure 4.** (**a**) Photocatalytic degradation curves of TC over different photocatalysts under visible light irradiation; (**b**) The pseudo-second-order kinetic curves of the as-prepared photocatalyst for the degradation of TC; (**c**) Photocatalytic degradation and (**d**) $k_2$ values of different TC concentration over F-BFTOC under visible light irradiation; (**e**) Photocatalytic degradation curves of RhB over different photocatalysts under visible light irradiation; (**f**) The pseudo-first-order kinetic curves of the as-prepared photocatalyst for the degradation of RhB; (**g**,**h**) Absorption spectra of TC and RhB photocatalyzed by F-BFTOC, respectively.

The stability of photocatalyst was the important factor for the practical application in wastewater treatments. The stability of F-BFTOC was measured for three consecutive cycles. The degradation activity of F-BFTOC did not decline substantially with no appreciable deactivation at the third cycle under visible light irradiation, which demonstrated that F-BFTOC had remarkable photocatalytic stability. XRD patterns of F-BFTOC photocatalyst before and after the degradation of TC were depicted in Figure S5. The XRD pattern of F-BFTOC after photodegradation testified that the locations of the characteristic diffraction peaks of BFTOC were not shifted and impurity was not observed. F-BFTOC was a kind of highly efficient and steady photocatalyst for the degradation of TC.

### *2.5. Degradation Pathway of TC and Toxicity Assessment of Products*

The intermediate products during the degradation of TC were identified by HPLC-MS and the possible degradation path of the TC over F-BFTOC was presented in Figure 5. Nine transformation products with $m/z$ of 461 (D), 433 (G), 306 (H), 146 (K), 106 (J), 164 (I), 431 (C), 298 (E), and 543 (F), and the corresponding molecular structures were observed. Two probable degradation pathways of TC were given. For pathway I, TC molecules were attacked by photoexcited $h^+$ to divide the N-demethylation into C. Then, C was fragmented into E via ring-opening process, and further transformed to F [43–45].

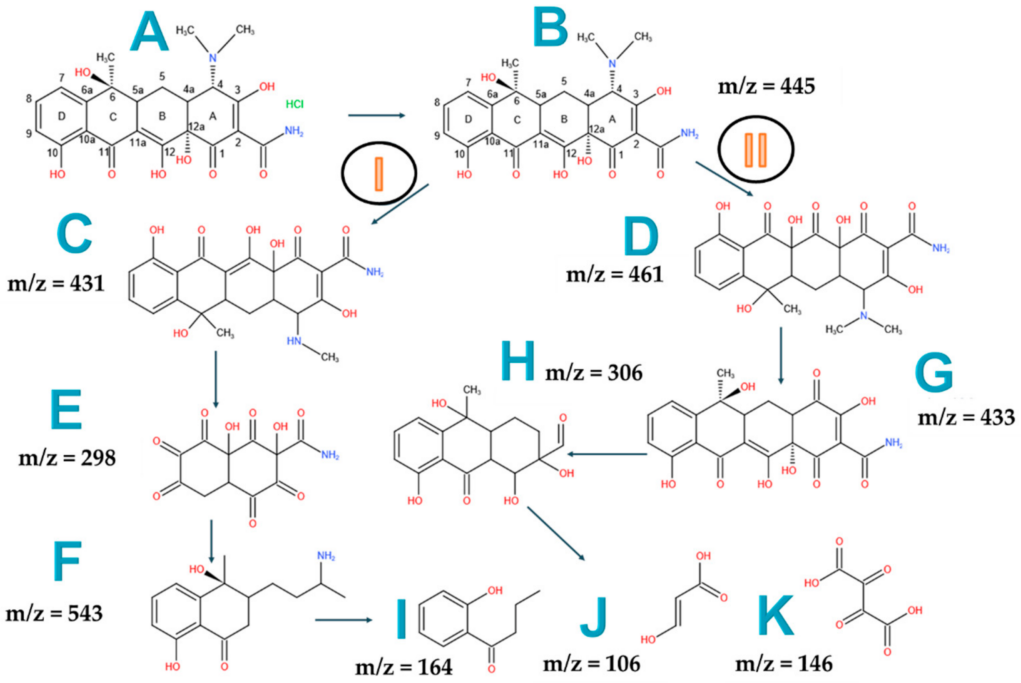


**Figure 5.** The proposed photodecomposition pathways of TC over F-BFTOC. (**A**–**K**) are tetracycline and different degradation products, respectively.

Pathway II was mainly fragmentation with the attack of $\cdot O_2^-$ active species, D was firstly formed by the dehydroxylation of TC. Then, the demethylation reaction occurred for D to generate G, and a small molecule H stemmed from deamination process. H was successively decomposed into intermediates J and K, corresponding to the ring opening reaction [46,47].

Afterwards, the I was gradually disintegrated into small molecule intermediates, and further converted into $CO_2$ and $H_2O$ [48].

Thanks to several intermediate products yielded during the photocatalytic degradation of TC, the mixture of intermediates was likely to have higher toxic properties. Therefore, the toxicity of the solution after photocatalytic treatment was supposed to be assessed in addition to the TC removal. The toxicities of products treated by F-BFTOC and the control

sample of TC solutions were shown in Figure 6. The blank group (pure water) allowed *E. coli* bacteria growth to some extent. A distinct bacteriostatic zone existed around the tetracycline hydrochloride discs, indicating that the high concentration of TC in the solution apparently hindered bacterial growth. Remarkably, a notable detoxification was achieved for some intermediate products, and a noticeable bacterial growth was observed, revealing the effective photocatalysis of TC by F-BFTOC led to a basically non-toxic environment. Thus, F-BFTOC could be used to degrade high concentrations of TC in the environment without producing more toxic products.

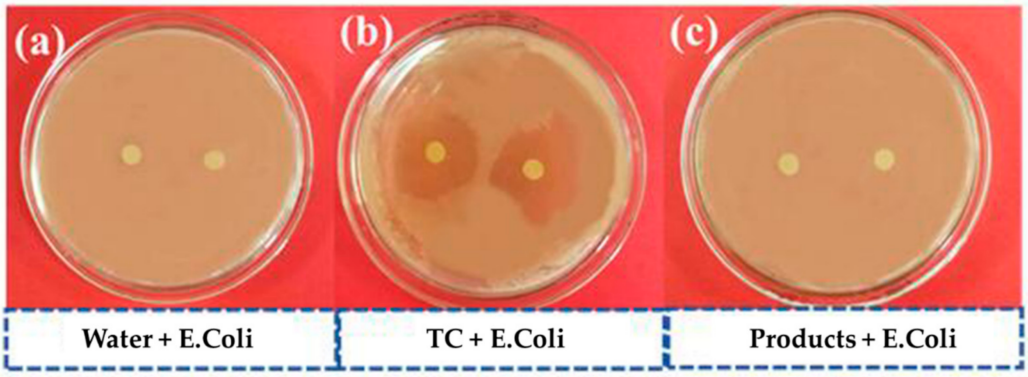


**Figure 6.** Toxicity assessment of (**a**) distilled water, (**b**) 50 mg/L TC and (**c**)products. The products came from TC degraded by F-BFTOC for 120 min.

### *2.6. Proposed Photocatalytic Mechanism*

For the purpose of elucidating the photoexcited charge separation efficiency of F-BFTOC, S-BFTOC, F-BNOC and S-BNOC, the photocurrent response (PC) and electrochemical impedance spectroscopy (EIS) were applied to investigate the recombination rate and migration process of the photogenerated charge carriers. The EIS Nynquist plots of the as-prepared photocatalysts were depicted in Figure 7a, a smaller EIS radius indicates a faster rate of electron migration, which is more favorable for photocatalysis. The arc radius of BFTOC was smaller than that of BNOC, which demonstrated the faster carries migration in the interface of BFTOC. More importantly, F-BFTOC possessed a smaller radius of semicircle in comparison to S-BFTOC. The transfer resistance of charge carriers in F-BFTOC was lower than S-BFTOC, suggesting that F-BFTOC effectively separated photogenerated electrons and holes. As presented in Figure 7b, the photocurrent density of BFTOC was significantly higher than BNOC, and F-BFTOC showed the strongest transient photocurrent intensity. F-BFTOC had the low recombination rate of the photogenerated electrons and holes via the formation of sheets structure by the appropriate flux route to enhance photon-to-current conversion efficiency.

To identify the generated reactive species during the photocatalytic degradation of RhB over F-BFTOC and speculate the probable photocatalytic mechanism, the active species trapping experiment of F-BFTOC was carried out by the addition of tert-butyl alcohol (*t*-BuOH), disodium ethylenediamine tetraacetate (EDTA-2Na) and p-benzoquinone (*p*-BQ) as trapping agents to quench radical ·OH, $h^+$, and superoxide radical $\cdot O_2^-$, respectively.

The concentration of each scavenger was 2 mmol/L. In Figure 7c, d, the degradation efficiency of RhB significantly reduced from 98% to 32%, 10% and 80% after adding *p*-BQ, EDTA-2Na, and *t*-BuOH, respectively. To confirm clearly the produced active species during the photodegradation procedure, the ESR spin-trap experiments were carried out by DMPO which acted as a spin-trapping agent. As illustrated in Figure 7e,f, no ESR signal of $\cdot O_2^-$ radicals appeared under dark conditions. In contrast, the photoexcitation of F-BFTOC under visible-light irradiation, the strong characteristic peaks of DMPO-$O_2^-$ were observed. Besides, the peak intensity of $h^+$ gradually decreased with the extension of the irradiation time, proving the reaction between TEMPO and $h^+$. To sum up, $h^+$ and $\cdot O_2^-$ radicals as the predominant active species participated in the photocatalytic degradation

process of pollutants performed over F-BFTOC. Although OH played a secondary role, it was still very important.

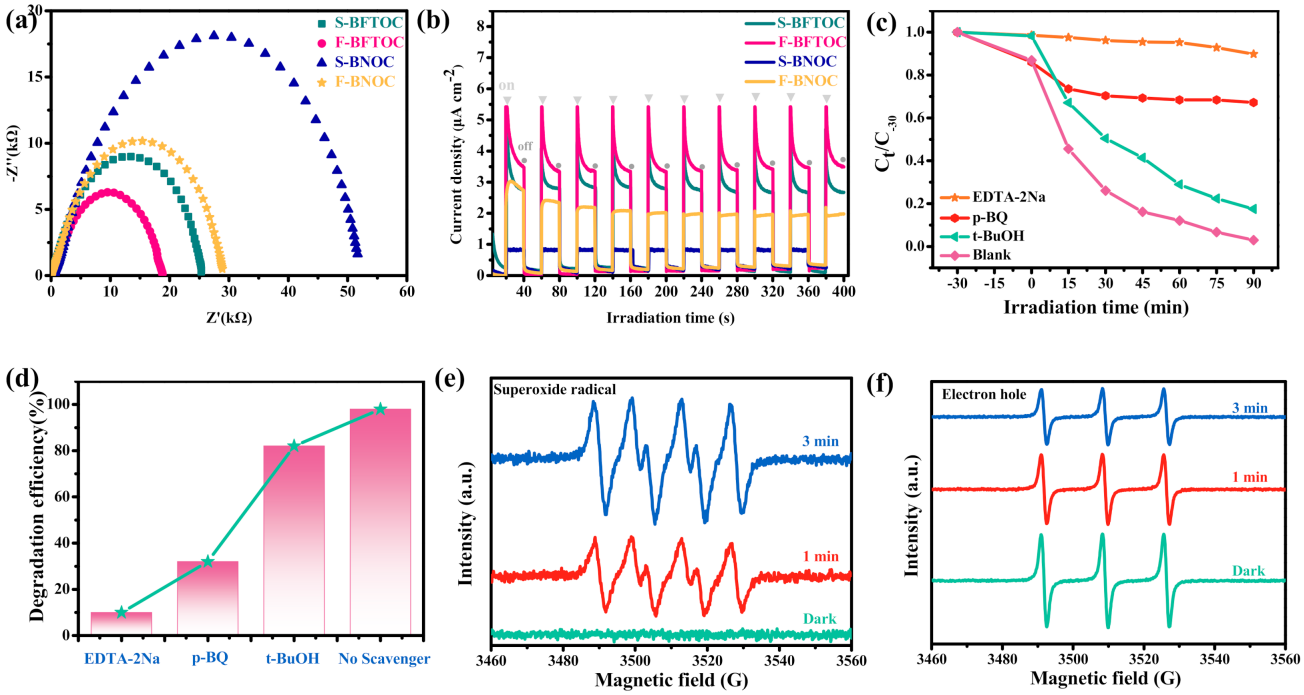


**Figure 7.** (**a**) EIS Nynquist plots of F-BFTOC, S-BFTOC, F-BNOC and S-BNOC, respectively; (**b**) Transient photocurrent densities of F-BFTOC, S-BFTOC, F-BNOC and S-BNOC, respectively; (**c**,**d**) The photocatalytic performance of F-BFTOC with different scavenges under visible light irradiation; (**e**) DMPO-$O_2^-$ spin-trapping ESR spectra of F-BFTOC; (**f**) TEMPO-$h^+$ spin-trapping ESR spectra of F-BFTOC.

According to the above results, the persuasive photocatalytic mechanisms for the degradation of TC or RhB over F-BFTOC was proposed and schematically described in Figure 8. Upon visible light irradiation, photo-induced electrons were blocked by the Schottky barrier. The photogenerated electrons ($e^-$) were activated and shifted to the conduction band (CB) while leaving more holes ($h^+$) on the valence band (VB) of F-BFTOC (Equation (4)), which was the main species for the degradation of TC/RhB. The photogenerated electrons would participate in the reduction in the dissolved oxygen ($O_2$) to superoxide radical anion ($\cdot O_2^-$) (Equation (6)), and the $\cdot O_2^-$ radicals was able to react with $H^+$ and electrons to further form $H_2O_2$. Afterwards, $H_2O_2$ could dissociate to radical OH under the action of electrons, and TC was decomposed by radical ·OH. Therefore, $\cdot O_2^-$ was the only transformation product and OH radicals were the finally product. The OH radicals conduced the conversion of TC/RhB into $CO_2$, $H_2O$, and other organic compounds (Equation (8)). The primary active species and the photocatalytic mechanism of TC/RhB over F-BFTOC were briefly described as follows:

$$\mathrm{BFTOC} + \mathrm{hv} \rightarrow \mathrm{BFTOC}\left(\mathrm{h}^+ + \mathrm{e}^-\right) \quad (4)$$

$$\mathrm{BFTOC}\left(\mathrm{h}^+\right) + \mathrm{OH}^- \rightarrow \mathrm{BFTOC} + \cdot\mathrm{OH} \quad (5)$$

$$\mathrm{BFTOC}\left(\mathrm{e}^-\right) + \mathrm{O}_2 \rightarrow \mathrm{BFTOC} + \cdot\mathrm{O}_2^- \quad (6)$$

$$\cdot\mathrm{O}_2^- + \mathrm{TC/RhB} \rightarrow \mathrm{CO}_2 + \mathrm{H}_2\mathrm{O} + \mathrm{mineral} \quad (7)$$

$$\mathrm{h}^+ + \mathrm{RhB/TC} \rightarrow \mathrm{CO}_2 + \mathrm{H}_2\mathrm{O} + \mathrm{mineral} \quad (8)$$

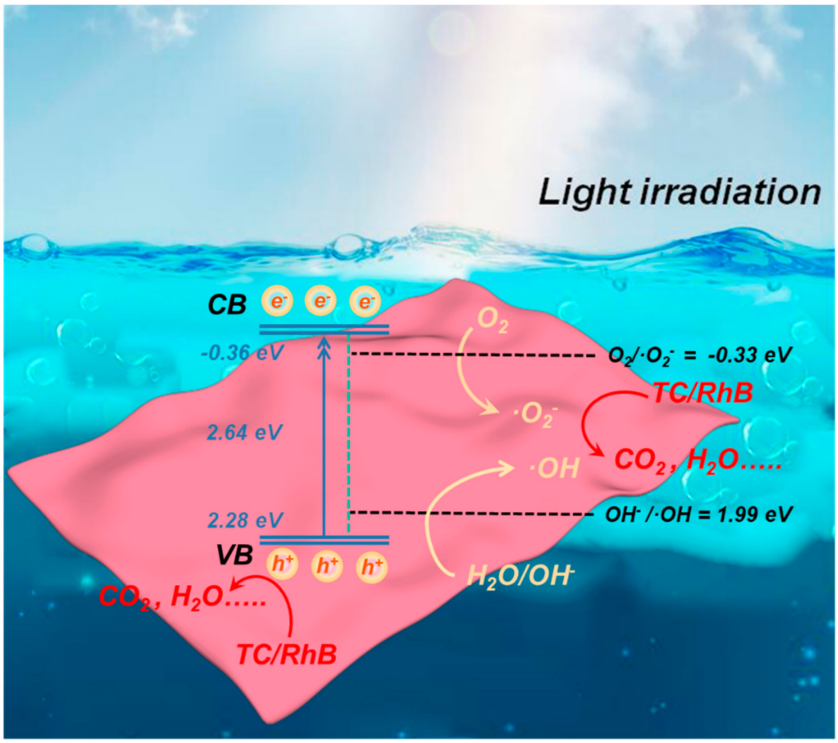


**Figure 8.** Schematic illustration of the proposed photocatalytic mechanism in the F-BFTOC for the degradation of TC/RhB.

## 3. Materials and Methods

### *3.1. Materials*

Bismuth trioxide ($Bi_2O_3$) was purchased from Aladdin reagent CO., Ltd., Shanghai, China. Ferric oxide ($Fe_2O_3$) was purchased from Shanghai shanpu chemical Co., Ltd., Shanghai, China. Titanium Dioxide ($TiO_2$), Polyethylene glycol (EG), Potassium chloride (KCl) and Sodium chloride (NaCl) were purchased from Sinopharm Chemical Reagent Co., Ltd., Shanghai, China. All of mentioned reagents were of analytical grade and directly used without further purification.

### *3.2. Preparation of BiOCl*

BiOCl was synthesized by a facile soft liquid deposition method. A total of 11.64 g $Bi(NO_3)_3{\cdot}5H_2O$ was dissolved into 240 mL glycol. Then, 1.78 g KCl was dissolved into 120 mL of deionized water, which was dropped slowly into the previous solution. The mixture was magnetically stirred at room temperature for 1 h. Subsequently, the products were obtained by washing with deionized water several times, and dried at 60 °C for 12 h.

### *3.3. Preparation of $Bi_7Fe_2Ti_2O_{17}Cl$*

$Bi_7Fe_2Ti_2O_{17}Cl$ was synthesized by a flux method using $Bi_2O_3$, $Fe_2O_3$, $TiO_2$ and BiOCl as raw materials. A molten salt of an alkali metal chloride KCl and NaCl was served as a flux. The flux was mixed with $Bi_2O_3$, BiOCl, $Fe_2O_3$ and $TiO_2$ at the stoichiometric molar ratio for $Bi_7Fe_2Ti_2O_{17}Cl$ (3:1:1:2), at a solute concentration ($Bi_7Fe_2Ti_2O_{17}Cl$/($Bi_7Fe_2Ti_2O_{17}Cl$ + flux)) of 6.25 mol%. Afterwards, the mixture was transferred to an alumina crucible with a capacity of 25 $cm^3$, calcined at 750 °C at a heating rate of 180 °C $h^{-1}$ for 12 h. After natural cooling, the obtained orange products were collected by filtration and thoroughly washed with deionized water. The powders were dried at 60 °C for 12 h, which was named as F-BFTOC. For comparison, $Bi_7Fe_2Ti_2O_{17}Cl$ was prepared by traditional solid-state method under the same condition without adding molten salt (other conditions were the same as the requirements of molten salt method), which was named as S-BFTOC.

### *3.4. Preparation of $Bi_4NbO_8Cl$*

$Bi_4NbO_8Cl$ were synthesized by a flux method. $Bi_2O_3$, BiOCl, and $Nb_2O_5$ were weighed at the stoichiometric molar ratio for $Bi_4NbO_8Cl$ (3:2:1). Take KCl and NaCl (30 mmol, respectively) as molten salt. Afterwards, the mixture was transferred to an alumina crucible, and calcined at 750 °C at a heating rate of 180 °C $h^{-1}$ for 12 h, which was named as F-BNOC. For comparison, $Bi_4NbO_8Cl$ was prepared by traditional solid-state method under the same condition without adding molten salt, which was named as S-BNOC.

### *3.5. Characterization*

X-ray diffraction (XRD) (X' Pert3 Powder, PANalytical, Almelo, the Netherlands, $\lambda$ = 0.15406 nm) was used to analyze the crystal structure of samples with a Cu K$\alpha$ radiation. The morphology of the samples was examined by field emission scanning electron microscope (FE-SEM) (FEI, Hillsboro, OR, USA). X-ray photoelectron spectroscopy (XPS) was carried out to investigate the chemical nature of the samples via a ESCALAB 250xi XPS system (Thermo Fisher Scientific, Carlsbad, CA, USA) with an Al K$\alpha$ X-ray source. The UV-vis diffuse reflectance spectroscopy (UV-vis DRS) was attained using a UV-2550 (Shimadzu, Kyoto, Japan) to measure the optical property. The liquid chromatography-triple quadrupole tandem mass spectrometry (HPLC-MS) (Agilent 6545Q-TOF, Singapore, Singapore) was utilized to test the intermediate products and study the photodegradation pathways. The electron spin resonance (ESR) signal was conducted by Bruker ESR A-300 (Bruker, Rheinstetten, Germany) to analyze the active species under visible light irradiation. The UV-Vis absorption spectra of the samples were performed by UV-2450 (Shimadzu, Kyoto, Japan).

### *3.6. Theoretical Calculations*

All the calculations in this work were implemented by the Vienna ab initio simulation package (VASP). The Perdew-Burke-Ernzerhof (PBE) [49] generalized gradient approximation (GGA) of density function theory (DFT) was conducted to optimize the geometric structure. The Brillouin zone grid was used to $5 \times 5 \times 1$ mesh and the energy cut off was 520 eV as well as $-0.01$ eV for atomic force convergence. Since the BFTOC is a strong correlation interaction system, the method of the Heyd-Scuseria-Ernzerhof screened hybrid functional (HSE) [50] was performed for the band structure calculations.

### *3.7. Photocatalytic Experiments*

Photocatalytic experiments of the samples were discussed, and a 300 W Xenon lamp (CEL-HXF300 Ceaulicht, Beijing, China) with a 420 nm filter as the visible light source, the current intensity was 20 A. A total 100 mg of photocatalysts was added into 100 mL of 10 mg $L^{-1}$ TC or RhB, and stirred in the dark for 30 min to reach adsorption-desorption equilibrium. An amount of 4 mL solution was withdrawn every 20 min (TC) or 15 min (RhB), then the above suspension was centrifuged, and the residual concentration of TC or RhB was detected by UV-vis spectrophotometer. The stability of F-BFTOC was tested under the same procedure.

### *3.8. Electrochemical Measurement*

Photocurrent density versus time curves and electrochemical impedance spectra (EIS) were performed by a CHI660D electrochemical analyser (Chenhua Instrument Co. Ltd., Shanghai, China) with a standard three-electrode system, including a working electrode, reference electrode (saturated Ag/AgCl) and counter electrode (Pt wire). The working electrode was obtained by the following procedure: 5 mg of as-prepared photocatalysts was dispersed into 40 µL of naphthol to make the slurry, and the slurry was deposited on the fluorine-tin oxide (FTO) glass. Then, the substrate was dried at 80 °C for 4 h and subsequently calcined in Muffle furnace (KF1100, Boyuntong Instrument Co., Ltd., Nanjing, China) at 120 °C for 1 h.

### *3.9. Toxicity Assessment*

The toxicity assessment of products was conducted by comparing the acute toxicity of the antibiotic solutions before and after photocatalytic treatment [51]. Prior to toxicity assessment, the bacteria were reactivated to the logarithmic growth phase.

Accordingly, the sterilized ultrapure water without TC was used as the medium in the control group. The TC solutions before and after being treated by photocatalysis at different times were employed for the test groups. The disk diffusion testing of *E. coli* on LB agar was performed [52]. In the experiment, three types of 6 mm paper discs were utilized: (1) paper disc saturated with distilled water; (2) tetracycline hydrochloride discs saturated with tetracycline hydrochloride solution (50 mg/L); and (3) products disks saturated with degraded products. *E. coli* strains were suspended in the saline solution and plated in the culture medium, and then the discs were placed. The plates were incubated at 37 °C for 12 h, and the inhibition zones were measured.

## 4. Conclusions

In summary, the Bi-based Sillén-Aurivillius $Bi_7Fe_2Ti_2O_{17}Cl$ was successfully fabricated by means of a one-step flux method. The F-BFTOC nanosheets exhibited more superior photocatalytic activity for the degradation of TC and RhB. As a result, 90% and 98% of degradation efficiency were achieved with 90 min or 60 min under visible light irradiation for refractory antibiotic TC and RhB, respectively. The excellent photocatalytic activity of F-BFTOC could be ascribed to the sheet-like structure that could expose more active sites and augment the contact area to accelerate the separation of the charge carriers. The photo-generated radical $\cdot O_2^-$ as a main active specie contributed to the degradation of TC. Under the attack of $\cdot O_2^-$ and $h^+$, TC was degraded by two possible pathways and nine probable intermediates were validated. Furthermore, the high efficiency of F-BFTOC retained after three cycles with slight and the intermediate products of TC had low toxicity. Overall, BFTOC as a multifunctional photocatalyst was capable of efficiently degrading persistent antibiotics and organic pollutants.

**Supplementary Materials:** The following supporting information can be downloaded at: https://www.mdpi.com/article/10.3390/catal12020221/s1, Figure S1: XRD patterns of F-BNOC and S-BNOC, Figure S2: XPS survey spectra of F-BFTOC corresponding to Bi, Fe, Ti, O and Cl, Figure S3: Ti 2p XPS spectrum of the $Bi_7Fe_2Ti_2O_{17}Cl$ sample, Figure S4: Cl 2p XPS spectrum of the $Bi_7Fe_2Ti_2O_{17}Cl$ sample, Figure S5: photocatalytic stability of TC degradation over F-BFTOC under visible light irradiation (a); XRD patterns of F-BFTOC photocatalyst before and after the degradation of TC (b), Figure S6: HPLC-MS chromatograms for monitoring the degradation of TC with F-BFTOC, Table S1: Linear Fit kinetics data of BFTOC and BNOC photocatalytic reaction, Table S2: Linear Fit kinetics data of BFTOC and BNOC photocatalytic reaction.

**Author Contributions:** Y.G.: Conceptualization, Methodology, Investigation, Testing, Writing-original draft. F.Y.: Writing-review & editing, Supervision, Data curation. J.C.: Theoretical Calculation, Validation. Q.Z.: Project administration, Funding acquisition, Writing-review & editing. All authors have read and agreed to the published version of the manuscript.

**Funding:** The work was supported by the Natural Science Foundation of Jiangsu Province (BK20211361 and BX2021054), College Natural Science Research Project of Jiangsu Province (20KJA430004) and the Postgraduate Research & Practice Innovation Program of Jiangsu Province (SJCX20_1239).

**Data Availability Statement:** The data presented in this study are available on request from the corresponding author.

**Conflicts of Interest:** The authors declare no conflict of interest.

## References


1. Mansingh, S.; Sultana, S.; Acharya, R.; Ghosh, M.K.; Parida, K.M. Efficient Photon Conversion via Double Charge Dynamics $CeO_2$-$BiFeO_3$ p-n Heterojunction Photocatalyst Promising toward $N_2$ Fixation and Phenol-Cr (VI) Detoxification. *Inorg. Chem.* **2020**, *59*, 3856–3873. [CrossRef] [PubMed]
2. Prete, P.; Fiorentino, A.; Rizzo, L.; Proto, A.; Cucciniello, R. Review of Aminopolycarboxylic Acids-Based Metal Complexes Application to Water and Wastewater Treatment by (Photo-)Fenton Process at Neutral pH. *Curr. Opin. Green. Sust.* **2021**, *28*, 100451. [CrossRef]
3. Zhou, J.; Ding, J.; Wan, H.; Guan, G. Boosting Photocatalytic Degradation of Antibiotic Wastewater by Synergy Effect of Heterojunction and Phosphorus Doping. *J. Colloid. Interf. Sci.* **2020**, *582*, 961–968. [CrossRef] [PubMed]
4. Roberto, F.; Balsamo, S.A.; D'Urso, L.; Sciré, S.; Brundo, M.V.; Pecoraro, R.; Scalisi, E.M.; Privitera, V.; Impellizzeri, G. $CeO_2$ for Water Remediation: Comparison of Various Advanced Oxidation Processes. *Catalysts* **2020**, *10*, 446.
5. Moradi, M.; Vasseghian, Y.; Khataee, A.; Harati, M.; Arfaeinia, H. Ultrasound-Assisted Synthesis of $FeTiO_3$/GO Nanocomposite for Photocatalytic Degradation of Phenol under Visible Light Irradiation. *Sep. Purif. Technol.* **2021**, *261*, 118274. [CrossRef]
6. Huang, B.; Li, N.X.; Lin, W.L.; Li, H. A Highly Ordered Honeycomb-Like Nickel (III/II) Oxide-enhanced Photocatalytic Fuel Cell for Effective Degradation of Bisphenol A. *J. Hazard. Mater.* **2018**, *360*, 578–586. [CrossRef]
7. Wang, D.; Jia, F.; Hou, W.; Fei, C.; Yuan, X. Simultaneously Efficient Adsorption and Photocatalytic Degradation of Tetracycline by Fe-Based MOFs. *J. Colloid Interf. Sci.* **2018**, *519*, 273–284. [CrossRef]
8. Lanzafame, P.; Centi, G.; Perathoner, S. Catalysis for Biomass and $CO_2$ Use through Solar Energy: Opening New Scenarios for A Sustainable and Low-Carbon Chemical Production. *Chem. Soc. Rev.* **2014**, *43*, 7562–7580. [CrossRef]
9. Kubacka, A.; Fernández-García, M.; Colón, G. Advanced Nanoarchitectures for Solar Photocatalytic Applications. *Chem. Rev.* **2016**, *112*, 1555–1614. [CrossRef]
10. Bhatkhande, D.S.; Pangarkar, V.G.; Beenackers, A.A.C.M. Photocatalytic Degradation for Environmental Applications-A Review. *J. Chem. Technol. Biot.* **2002**, *77*, 102–116. [CrossRef]
11. Fujishima, A.; Honda, K. Electrochemical Photocatalysis of Water at Semiconductor Electrode. *Nature* **1972**, *238*, 37–38. [CrossRef] [PubMed]
12. Dutta, V.; Sharma, S.; Raizada, P.; Thakur, V.K.; Singh, P. An Overview on $WO_3$ Based Photocatalyst for Environmental Remediation. *J. Environ. Chem. Eng.* **2021**, *14*, 2519–2542. [CrossRef]
13. Lu, X.W.; Li, X.Z.; Chen, F.; Chen, Z.G.; Zhang, Q.F. Biotemplating Synthesis of N-Doped Two-Dimensional $CeO_2$-$TiO_2$ Nanosheets with Enhanced Visible Light Photocatalytic Desulfurization Performance. *J. Alloys Compd.* **2019**, *815*, 152326. [CrossRef]
14. Zhang, F.; Zhuang, H.Q.; Zhang, W.M.; Yin, J.; Cao, F.H.; Pan, Y.-X. Noble-Metal-Free CuS/CdS Photocatalyst for Efficient Visible-Light-Driven Photocatalytic $H_2$ Production from Water. *Catal. Today* **2019**, *330*, 203–208. [CrossRef]
15. Zhuang, J.; Tian, Q.; Lin, S.; Yang, W.; Chen, L.; Liu, P. Precursor Morphology-Controlled Formation of Perovskites $CaTiO_3$ and Their Photo-Activity for As (III) Removal. *Appl. Catal. B-Environ.* **2014**, *156*, 108–115. [CrossRef]
16. Han, N.; Xu, Q.X.; Beyene, G.; Zhang, Q.F. Enhanced Photocatalytic Activity over g-$C_3N_4$/$(BiO)_2(OH)_xCl_{2-x}$ Z-Scheme Heterojunction. *Appl. Surf. Sci.* **2020**, *521*, 146464. [CrossRef]
17. Bahers, T.L.; Rérat, M.; Sautet, P. Semiconductors Used in Photovoltaic and Photocatalytic Devices: Assessing Fundamental Properties from DFT. *J. Phys. Chem. C* **2014**, *118*, 5997–6008. [CrossRef]
18. Samsudin, M.F.R.; Ullah, H.; Bashiri, R.; Mohammed, N.M.; Yun, H.N. Experimental and DFT Insights on Microflower g-$C_3N_4$/$BiVO_4$ Photocatalyst for Enhanced Photoelectrochemical Hydrogen Generation from Lake Water. *ACS Sustain. Chem. Eng.* **2020**, *8*, 9393–9403. [CrossRef]
19. Zhang, L.S.; Wang, W.Z.; Yang, J.; Chen, Z.G.; Zhou, W.Q.L.; Liu, S.W. Sonochemical Synthesis of Nanocrystallite $Bi_2O_3$ as a Visible-Light-Driven Photocatalyst. *Appl. Catal. A-Gen.* **2006**, *308*, 105–110. [CrossRef]
20. Zhang, X.; Ai, Z.; Jia, F.; Zhang, L. Generalized One-Pot Synthesis, Characterization, and Photocatalytic Activity of Hierarchical BiOX (X = Cl, Br, I) Nanoplate Microspheres. *J. Phys. Chem. C* **2008**, *112*, 747–753. [CrossRef]
21. Zhang, L.; Wang, W.; Zhou, L.; Xu, H. $Bi_2WO_6$ Nano- and Microstructures: Shape Control and Associated Visible-Light-Driven Photocatalytic Activities. *Small* **2010**, *3*, 1618–1625. [CrossRef] [PubMed]
22. Peng, Y.-H.; Zhang, Y.; Tian, F.H.; Zhang, J.Q.; Yu, J.Q. Structure Tuning of $Bi_2MoO_6$ and Their Enhanced Visible Light Photocatalytic Performances. *Crit. Rev. Solid State Mater. Sci.* **2017**, *42*, 1–26. [CrossRef]
23. Xu, L.; Wan, Y.P.; Xie, H.D.; Huang, Y.L.; Qiao, X.B.; Qin, L.; Seo, H.J. On Structure, Optical Properties and Photodegradated Ability of Aurivillius-Type $Bi_3TiNbO_9$ Nanoparticles. *J. Am. Ceram. Soc.* **2016**, *99*, 3964–3972. [CrossRef]
24. Fujito, H.; Kunioku, H.; Kato, D.; Suzuki, H.; Higashi, M.; Kageyama, H.; Abe, R. Layered Perovskite Oxychloride $Bi_4NbO_8Cl$: A Stable Visible Light Responsive Photocatalyst for Water Splitting. *J. Am. Chem. Soc.* **2016**, *47*, 2082–2085. [CrossRef] [PubMed]
25. Zhen, S.; Zhu, L.; Dong, Z.; Fan, L.; Wang, B.; Zhang, Q.F. A New Bi-Based Oxychloride $Bi_4Ti_{0.5}W_{0.5}O_8Cl$ as a Photocatalyst. *Catal. Lett.* **2018**, *148*, 2480–2486. [CrossRef]
26. Meng, X.C.; Zhang, Z.S. Facile Synthesis of BiOBr/$Bi_2WO_6$ Heterojunction Semiconductors with High Visible-Light-Driven Photocatalytic Activity. *J. Photochem. Photobiol. A* **2015**, *310*, 33–44. [CrossRef]
27. Ozaki, D.; Suzuki, H.; Ogawa, K.; Sakamoto, R.; Inaguma, Y.; Nakashima, K.; Tomita, O.; Kageyama, H.; Abe, R. Synthesis, Band Structure and Photocatalytic Properties of Sillén–Aurivillius Oxychlorides $BaBi_5Ti_3O_{14}Cl$, $Ba_2Bi_5Ti_4O_{17}Cl$ and $Ba_3Bi_5Ti_5O_{20}Cl$ with Triple-, Quadruple- and Quintuple-perovskite Layers. *J. Mater. Chem. A* **2021**, *9*, 8332–8340. [CrossRef]

28. Nakada, A.; Saeki, A.; Higashi, M.; Kageyama, H.; Abe, R. Two-step synthesis of Sillén-Aurivillius Type Oxychlorides to Enhance Their Photocatalytic Activity for Visible-Light-Induced Water splitting. *J. Mater. Chem. A* **2018**, *6*, 10909–10917. [CrossRef]
29. Majumdar, A.; Ghosh, U.; Pal, A. Novel 2D/2D g-$C_3N_4$/$Bi_4NbO_8Cl$ Nano-Composite for Enhanced Photocatalytic Degradation of Oxytetracycline under Visible LED Light Irradiation. *J. Colloid Interface Sci.* **2021**, *584*, 320–331. [CrossRef]
30. Wei, Z.; Liu, J.; Shangguan, W. A Review on Photocatalysis in Antibiotic Wastewater: Pollutant Degradation and Hydrogen Production. *Chin. J. Catal.* **2020**, *41*, 1440–1450. [CrossRef]
31. Xu, Y.; You, Y.; Huang, H.W.; Guo, Y.X.; Zhang, Y.H. $Bi_4NbO_8Cl$ {001} Nanosheets Coupled with g-$C_3N_4$ as 2D/2D Heterojunction for Photocatalytic Degradation and $CO_2$ Reduction. *J. Hazard. Mater.* **2020**, *381*, 121159. [CrossRef] [PubMed]
32. Wu, X.L.; Zhang, Y.L.; Wang, K.; Zhang, S.; Qu, X.F.; Shi, L.; Du, F.-L. In-Situ Construction of Bi/Defective $Bi_4NbO_8Cl$ for Non-noble Metal Based Mott-Schottky Photocatalysts towards Organic Pollutants Removal. *J. Hazard. Mater.* **2020**, *393*, 122408. [CrossRef] [PubMed]
33. Chen, Z.; Hong, T.; Wang, Z.; Wang, J.; Huang, H.; Peng, R.; Yan, W.; Fu, Z.; Brinkman, K.S.; Lu, Y. Anisotropic Magnetic Property and Exchange Bias Effect in a Homogeneous Sillén-Aurivillius Layered Oxide. *J. Eur. Ceram. Soc.* **2019**, *39*, 2685–2691. [CrossRef]
34. Zhu, X.D.; Wang, Y.J.; Sun, R.J.; Zhou, D.M. Photocatalytic Degradation of Tetracycline in Aqueous Solution by Nanosized $TiO_2$. *Chemosphere* **2013**, *92*, 925–932. [CrossRef]
35. Ding, J.; Dai, Z.; Qin, F.; Zhao, H.; Zhao, S.; Chen, R. Z-Scheme $BiO_{1-x}Br/Bi_2O_2CO_3$ Photocatalyst with Rich Oxygen Vacancy as Electron Mediator for Highly Efficient Degradation of Antibiotics. *Appl. Catal. B Environ.* **2017**, *205*, 281–289. [CrossRef]
36. Lu, L.W.; Lv, M.L.; Wang, D.; Liu, G.; Xu, X.X. Efficient Photocatalytic Hydrogen Production over Solid Solutions $Sr_{1-x}Bi_xTi_{1-x}Fe_xO_3$ ($0 \leq x \leq 0.5$). *Appl. Catal. B Environ.* **2017**, *200*, 412–419. [CrossRef]
37. Jiang, L.; Ni, S.; Liu, G.; Xu, X.X. Photocatalytic Hydrogen Production over Aurivillius Compound $Bi_3TiNbO_9$ and Its Modifications by Cr/Nb Co-Doping. *Appl. Catal. B Environ.* **2017**, *217*, 342–352. [CrossRef]
38. Hu, J.; Fan, W.; Ye, W.; Huang, C.; Qiu, X. Insights into the Photosensitivity Activity of BiOCl under Visible Light Irradiation. *Appl. Catal. B Environ.* **2014**, *158–159*, 182–189. [CrossRef]
39. Ogawa, K.; Nakada, A.; Suzuki, H.; Tomita, O.; Higashi, M.; Saeki, A.; Kageyama, H.; Abe, R. Flux Synthesis of Layered Oxyhalide $Bi_4NbO_8Cl$ Photocatalyst for Efficient Z-Scheme Water Splitting under Visible Light. *ACS Appl. Mater. Inter.* **2018**, *11*, 5642–5650. [CrossRef]
40. Tauc, J. Optical Properties and Electronic Structure of Amorphous Germanium. *Mater. Res. Bull.* **1968**, *3*, 37–46. [CrossRef]
41. Davis, A.P.; Hao, O.-J. Reactor Dynamics in the Evaluation of Photocatalytic Oxidation Kinetics. *J. Catal.* **1991**, *131*, 285–288. [CrossRef]
42. Ning, D.; Zhang, L.; Hashimoto, M.; Iwasaki, K.; Meng, Q.-B. Enhanced Photocatalytic Activity of Mesoporous Carbon/$C_3N_4$ Composite Photocatalysts. *J. Colloid Interface Sci.* **2018**, *512*, 474–479.
43. Yang, Y.; Zeng, Z.; Zhang, C.; Huang, D.; Zeng, G.; Xiao, R.; Lai, C.; Zhou, C.; Guo, H.; Xue, W. Construction of Iodine Vacancy-rich BiOI/Ag@AgI Z-Scheme Heterojunction Photocatalysts for Visible-Light-Driven Tetracycline Degradation: Transformation Pathways and Mechanism Insight. *Chem. Eng. J.* **2018**, *349*, 808–821. [CrossRef]
44. Zhang, Y.; Zhou, J.B.; Chen, X.; Wang, L.; Cai, W.Q. Coupling of Heterogeneous Advanced Oxidation Processes and Photocatalysis in Efficient Degradation of Tetracycline Hydrochloride by Fe-Based MOFs: Synergistic effect and Degradation Pathway. *Chem. Eng. J.* **2019**, *369*, 745–757. [CrossRef]
45. Bell, N.J.; Ng, Y.H.; Du, A.; Coster, H.; Smith, S.C.; Amal, R. Understanding the Enhancement in Photoelectrochemical Properties of Photocatalytically Prepared $TiO_2$-Reduced Graphene Oxide Composite. *J. Phys. Chem. C* **2011**, *115*, 6004–6009. [CrossRef]
46. Xie, L.; Yang, Z.; Xiong, W.; Zhou, Y.; Cao, J.; Peng, Y.; Li, X.; Zhou, C.; Xu, R.; Zhang, Y. Construction of MIL-53(Fe) Metal-organic Framework Modified by Silver Phosphate Nanoparticles as a Novel Z-scheme Photocatalyst: Visible-Light Photocatalytic Performance and Mechanism Investigation. *Appl. Surf. Sci.* **2019**, *465*, 103–115. [CrossRef]
47. Shi, Q.; Zhang, Y.; Sun, D.; Zhang, S.; Cao, S. $Bi_2O_3$-Sensitized $TiO_2$ Hollow Photocatalyst Drives the Efficient Removal of Tetracyclines under Visible Light. *Inorg. Chem.* **2020**, *59*, 18131–18140. [CrossRef]
48. Majumdar, A.; Pal, A. Optimized Synthesis of $Bi_4NbO_8Cl$ Perovskite Nanosheets for Enhanced Visible Light Assisted Photocatalytic Degradation of Tetracycline Antibiotics. *J. Environ. Chem. Eng.* **2020**, *8*, 103645. [CrossRef]
49. Perdew, J.P.; Burke, K.; Ernzerhof, M. Generalized Gradient Approximation Made Simple. *Phys. Rev. Lett.* **1996**, *77*, 3865. [CrossRef]
50. Heyd, J.; Scuseria, G.E.; Ernzerhof, M. Hybrid Functionals Based on a Screened Coulomb Potential. *J. Chem. Phys.* **2003**, *118*, 8207–8215. [CrossRef]
51. Chen, C.; Zeng, H.; Yi, M.; Xiao, G.; Xu, S.; Shen, S.; Bo, F. In-Situ Growth of $Ag_3PO_4$ on Calcined Zn-Al Layered Double Hydroxides for Enhanced Photocatalytic Degradation of Tetracycline under Simulated Solar Light Irradiation and Toxicity Assessment. *Appl. Catal. B Environ.* **2019**, *252*, 47–54. [CrossRef]
52. Afranio, C.F.; Rocha, M.K.; Jucá, M.E.J.; Oliveira, C.M.C.S.; Martins, M.A.A.; De, S.I.P.; Albuquerque, M.E.; Almeida, F.P.B. Silver Nanoparticles-Disk Diffusion Test Against Escherichia Coli Isolates. *Rev. Inst. Med. Trop. Sao Paulo* **2016**, *58*, 73.